Check for updates

View Article Online
View Journal

Journal of
Materials Chemistry C

Materials for optical, magnetic and electronic devices

Accepted Manuscript

This article can be cited before page numbers have been issued, to do this please use: M. Anandan, S. Nasiri, P. Managutti, S. Mohamed, J. Padgurskas, R. Rukuiža, J. Nunzi, V. Nutalapati and Y. Li, *J. Mater. Chem. C*, 2026, DOI: 10.1039/D6TC01665K.

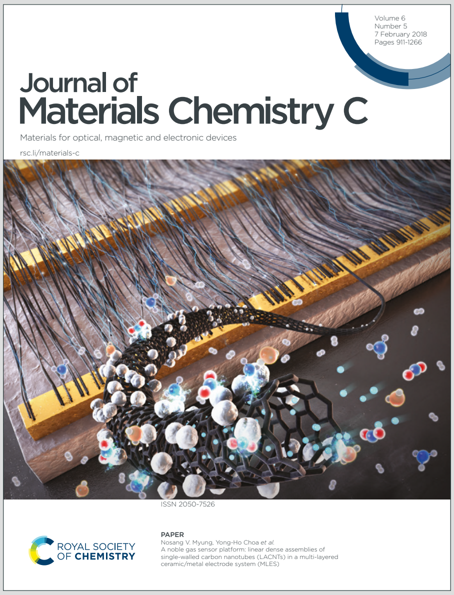

Volume 6
Number 5
7 February 2018
Pages 911-1266

Journal of
Materials Chemistry C
Materials for optical, magnetic and electronic devices
rsc.li/materials-c

ISSN 2050-7526

ROYAL SOCIETY
OF CHEMISTRY

PAPER
Nosang V. Myung, Yong-Ho Choa *et al.*
A noble gas sensor platform: linear dense assemblies of single-walled carbon nanotubes (LACNTs) in a multi-layered ceramic/metal electrode system (MLES)

This is an Accepted Manuscript, which has been through the Royal Society of Chemistry peer review process and has been accepted for publication.

Accepted Manuscripts are published online shortly after acceptance, before technical editing, formatting and proof reading. Using this free service, authors can make their results available to the community, in citable form, before we publish the edited article. We will replace this Accepted Manuscript with the edited and formatted Advance Article as soon as it is available.

You can find more information about Accepted Manuscripts in the Information for Authors.

Please note that technical editing may introduce minor changes to the text and/or graphics, which may alter content. The journal's standard Terms & Conditions and the Ethical guidelines still apply. In no event shall the Royal Society of Chemistry be held responsible for any errors or omissions in this Accepted Manuscript or any consequences arising from the use of any information it contains.

ROYAL SOCIETY
OF CHEMISTRY

rsc.li/materials-c

View Article Online
DOI: 10.1039/D6TC01665K

ARTICLE

Tuning the space and charge in molecular delocalization of Highly Efficient Blue TADF Emitters Based on a 3,4,6,7,9,10-Hexahydroacridine-1,8(2H,5H)-dione Acceptor

Received 00th January 20xx,
Accepted 00th January 20xx

DOI: 10.1039/x0xx00000x

Mageshwari Anandan[a], Sohrab Nasiri[b,d]*, Praveen B. Managutti[c], Sharmarke Mohamed[c], Juozas Padgurskas[d], Raimundas Rukuiza[d], Jean Michel Nunzi [e], Yuning Li[b]*, Venkatramaiah Nutalapati[af]*

Development of stable and efficient blue thermally activated delayed fluorescence (TADF) emitters remains challenging due to intrinsic trade-offs among high excited-state energy, small singlet-triplet energy splitting (ΔE_{ST}), suppressed nonradiative decay, and solid-state morphological stability. A major limitation lies in the scarcity of acceptor units that simultaneously enable deep-blue emission, conformational rigidity, and resistance to aggregation-induced quenching. Here, we introduce saturated 3,4,6,7,9,10-hexahydroacridine-1,8-dione (**HHAD**) as an unconventional acceptor for blue TADF emitters. Unlike conventional planar acceptors, HHAD combines strong electron-withdrawing carbonyl groups with an intrinsically nonplanar and rigid framework. Two phenyl-bridged donor-π-acceptor emitters incorporating carbazole donors were designed to regulate intramolecular motion through linkage topology. Single-crystal X-ray diffraction reveals twisted donor–acceptor geometries with suppressed π-π stacking. Consequently, both emitters exhibit aggregation-induced emission, solid-state photoluminescence quantum yields exceeding 80%, and small ΔE_{ST} values down to 0.06 eV, enabling efficient reverse intersystem crossing. The neat emitter device exhibits pure blue emission with CIE coordinates of (0.179, 0.183). Upon optimization in a DPEPO host matrix, the device achieves an external quantum efficiency of 19.71%, a peak brightness of 48,859 cd m-2, and a turn-on voltage below 3.06 V. These results demonstrate that conformationally engineered HHAD acceptors offer an effective platform for high-performance blue TADF emitters.

Introduction

Organic light-emitting diodes (OLEDs) have rapidly become a leading display technology in modern consumer electronics, including smartwatches, smartphones and televisions, and are increasingly being adopted in the automotive industry.[1] Among the primary colour components, blue OLEDs still lag their red and green counterparts due to inherently lower efficiency, poorer stability, and broader emission spectra.[2,3] Blue OLEDs require higher singlet exciton energies and suffer from the low photopic sensitivity of human vision to blue light.[4] These factors lead to significantly greater power demands, elevated excitonic and thermal stress, and ultimately accelerated material degradation. As a result, the development of long-lived, high-efficiency blue emitters remain one of the most pressing challenges in OLED display technology and a major focus of ongoing research.[5] In contrast to phosphorescent emitters, which rely on heavy metal complexes to utilize triplet excitons, organic thermally activated delayed fluorescence (TADF) dyes are metal-free and therefore offer a cost-effective and environmentally friendly alternative. TADF emitters can theoretically achieve 100% internal quantum efficiency (IQE) by converting triplet excitons into singlets via reverse intersystem crossing (RISC). However, since RISC is thermally activated, its efficiency is highly temperature-dependent, often limiting performance at lower temperatures.[6,7] Particularly, designing efficient deep-blue TADF emitters remains a significant challenge because 1) achieving a small singlet-triplet energy gap (ΔE_{ST}) becomes increasingly difficult at higher energies; 2) the spatial separation between the highest occupied molecular orbital (HOMO) and the lowest unoccupied molecular orbital (LUMO) reduces the oscillator strength and photoluminescence quantum yield (PLQY); 3) high-energy blue photons accelerate material degradation; and 4) there is an inherent trade-off between efficiency, color purity, and device lifetime.[8,9] To overcome these challenges, donor-acceptor (D-A) molecules with spatially separated HOMO and LUMO have been developed. Their electronic structures must be precisely tuned to preserve strong radiative transitions while suppressing non-radiative decay pathways.[10] Additionally, rigid and thermally stable molecular frameworks help minimize vibrational relaxation and enhance device durability,[11-13] while bulky substituents mitigate aggregation-caused quenching (ACQ) and preserve emission color purity in the solid state.[14,15] Acceptor building blocks play a critical role in achieving efficient deep blue emitters, with electroluminescence (EL) emission wavelengths below 490 nm.[16] A wide range of acceptor units have been extensively explored, including triazine (TRz), pyrazine, pyrimidine, boron-based moieties, nitrile (CN)-substituted benzenes, oxadiazoles, sulfones, and ketone-functionalized aromatics. Among these, TADF blue emitters incorporating boron-based acceptors have

---

[a] *Functional Materials Laboratory, Department of Chemistry, Faculty of Engineering and Technology, SRM Institute of Science and Technology, Kattankulathur, Tamil Nadu-603203, India*
[b] *Department of Chemical Engineering and Waterloo Institute for Nanotechnology (WIN), University of Waterloo, QNC-5621, 200 University Ave West, Waterloo, Ontario N2L 3G1, Canada*
[c] *Chemical Crystallography Laboratory, Khalifa University of Science and Technology, Abu Dhabi, PO Box 127788, United Arab Emirates.*
[d] *Department of Mechanical, Energy and Biotechnology Engineering, Vytautas Magnus University, Akademija, LT-53361 Kauno r, Lithuania*
[e] *Department of Physics, Engineering Physics & Astronomy, Queens University, Kingston K7L-3N6, Ontario, Canada*
[f] *Centre for Interdisciplinary Research (CIDR), SRM University-AP, Amaravati, Andhra Pradesh 522 240, India*

† Footnotes relating to the title and/or authors should appear here.

View Article Online
DOI: 10.1039/D6TC01665K

demonstrated the best color purity and device efficiency, while triazine-based emitters have shown superior device stability.[16-19] Nevertheless, the overall performance of current blue TADF emitters remains inadequate for practical applications, highlighting the need for continued development of novel acceptor building blocks to further enhance device efficiency, stability, and emission characteristics. 9,10-Dihydroacridine (DHACR), which contains an electron-donating bridging nitrogen atom, is a well-known electron-donating building block for TADF emitters,[16] particularly for several high-performing blue emitters (**Figure 1a**).[20-23] In contrast, its saturated analog, 3,4,5,6,7,9-hexahydro-1H-10λ^2-acridine-1,8(2H)-dione (HHAD), retains the same core framework but incorporates two ketone groups, rendering it an electron-accepting building block. Although HHAD derivatives have been investigated in dyes, pharmaceuticals, optical materials, and catalysts,[24-26] their application in OLEDs remains largely unexplored. Recently, we employed HHAD as an acceptor building block to develop three host materials, achieving a high external quantum efficiency (EQE) of up to 13% when a green TADF emitter 9-[4-(4,6-diphenyl-1,3,5-triazin-2-yl)phenyl]-N3,N3,N6,N6-tetraphenyl-9H-carbazole-3,6-diamine (DACT-II) was used.[27] Notably, these HHAD-based compounds exhibited high and balanced hole and electron mobilities, with space-charge-limited current (SCLC) values on the order of ~10^{-4} to 10^{-3} cm^2 V^{-1} s^{-1}, which significantly contributed to enhanced device performance. Building on recent advances, this study employs HHAD as an acceptor and 9-phenyl-9H-carbazole (CzPh) as a donor to design two isomeric D–A type blue TADF emitters: **Dye 1** and **Dye 2** (**Figure 1b**). In **Dye 1**, a phenylene spacer connects the *para*-position of the N-phenyl group in CzPh to the C-9 position of HHAD. In **Dye 2**, the same spacer links the 3-position of the carbazole core directly to C-9 of HHAD. Both dyes exhibit deep blue emissions, with optical energy gaps of 2.66 eV (**Dye 1**) and 2.98 eV (**Dye 2**). They also possess small ΔE_{ST} values 0.07 and 0.06 eV, respectively, features conducive to efficient reverse intersystem crossing and blue TADF behavior.[28,29] Structurally, **Dye 1** contains two freely rotating bonds between the HHAD acceptor and the carbazole donor: one between the phenylene spacer and the N-phenyl group, and another between the N-phenyl group and the carbazole core. In contrast, **Dye 2** has only one such rotatable bond, between the phenylene spacer and the carbazole. This makes **Dye 2** more conformationally rigid, which helps suppress intramolecular motions, enhances electronic coupling, and reduces non-radiative decay.

As a result, **Dye 2** delivers significantly better device performance than **Dye 1**. In OLED devices, **Dye 2** emits blue light with CIE coordinates of (0.179, 0.183), achieving a maximum external quantum efficiency (EQE) of 19.71%, a peak brightness of 48,859 cd.m^{-2}, and a low turn-on voltage below 3.06 V. The exceptionally high brightness provides substantial headroom, enabling operation at low drive voltages under typical conditions (e.g., <1000 cd.m^{-2}), which helps extend device lifetime.[30] This performance also makes **Dye 2** well-suited for outdoor applications, micro displays, AR/VR systems, and specialized lighting applications where high luminance is critical.[31,32] Compared to other blue TADF emitters based on established acceptor building blocks (**Table S6**), our materials exhibit not only competitive brightness but also superior performance across key parameters, including EQE, color purity, turn-on voltage, and power efficiency. These results underscore the potential of HHAD as promising acceptor building blocks for the development of high-performance blue TADF emitters with strong prospects for practical applications. Despite significant progress in TADF dyes, the development of highly efficient and stable blue emitters remains a major challenge. Efficient blue TADF emitters must simultaneously possess a high excited-state energy, a small ΔE_{ST}, high PLQY, strong resistance to aggregation-caused quenching, and excellent thermal and morphological stability. However, these requirements are often mutually conflicting. Many existing acceptor units either fail to provide sufficiently deep-blue emission or suffer from increased non-radiative losses, limited molecular rigidity, and poor solid-state performance. Therefore, identifying new acceptor building blocks capable of balancing excited-state energy, singlet–triplet energy splitting, molecular rigidity, and solid-state emission efficiency remains a critical challenge in the development of next-generation blue TADF materials. In this work, we address this challenge by introducing HHAD as a novel acceptor building block and investigating how conformational engineering can improve blue TADF performance, aggregation behavior, and OLED device efficiency.

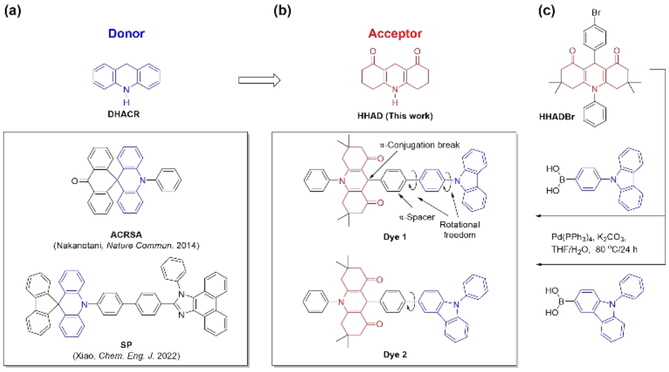

Figure 1. (a) Representative thermally activated delayed fluorescence (TADF) blue emitters incorporating DHACR as the donor unit. (b) Molecular structures of **Dye 1** and **Dye 2** developed in this work, in which HHAD serves as the acceptor unit. (c) Synthetic routes to **Dye 1** and **Dye 2** via Suzuki coupling reactions.

Results and discussion

Synthesis and Characterization of Dyes

Prior to synthesis, density functional theory (DFT) and time-dependent DFT (TD-DFT) calculations were carried out to investigate the electronic structures of the two dyes. Geometry optimizations of the isolated molecules were first performed at the ground state using the B3LYP functional.[33] The optimized structures were subsequently employed in TD-DFT calculations to determine the excited-state energy levels, using the same basis set. As illustrated in **Figure S11**, the HOMOs are primarily localized on the carbazole donor units, while the LUMOs are predominantly distributed over the HHAD acceptor moieties. This spatial separation between the HOMO and LUMO is a key molecular design feature that minimizes the exchange interaction between the electron and hole, thereby enhancing the resonance effect and achieving a small ΔE_{ST}, which is essential for efficient RISC.[13,34] The DFT calculated HOMO and LUMO energy levels are summarized in **Table 1**. Compared to Dye 1, Dye 2 exhibits elevated HOMO and LUMO energy levels as well as a larger band gap. Dye 1 and Dye 2 were synthesized in moderate yields (48% and 41%, respectively) via Pd-catalyzed Suzuki-Miyaura coupling of the corresponding CzPh-derived boronic acids with HHADBr **(Figure 1c).** HHADBr was prepared in one pot by condensing dimedone, 4-bromobenzaldehyde, and aniline (**Scheme S1).** Their structures were confirmed by ^1H and ^{13}C NMR **(Figure S1-S4)** and high-resolution mass spectrometry (HRMS) **(Figure S7-S8).**

View Article Online
DOI: 10.1039/D6TC01665K

Table 1. Thermal and optoelectronic properties of **Dye 1** and **Dye 2**.

Dye	T_m/T_d, °C	DFT E_{HOMO}/E_{LUMO}, eV	CV ^{a}IP/EA, eV	$\lambda_{max, abs}$, nm THF/Tol/Film	$\lambda_{max, em}$, nm THF/Tol/Film	PLQY, % THF/Tol/Film	$E_{g\ opt}$, eV Film
Dye 1	277/439	-5.43/-1.88	5.72/3.06	256/256/255	422/449/466	1/5/44	2.66
Dye 2	286/452	-5.32/-1.75	5.59/2.61	294/285/251	422/455/439	11/3/57	2.98

(a) IP values were calculated by the formula [-($E_{\text{onset of oxidation}}$+4.8)],[35,36] while EA values were determined using EA_{CV}= (IP_{CV}+E_g^{opt}).

Thermal properties of synthesized dyes were evaluated using derivative thermogravimetry (DTG) and differential scanning calorimetry (DSC) (**Figure S12** and **Table 1**). DSC measurements reveal high melting temperatures (T⍰) of 277 °C for **Dye 1** and 286 °C for **Dye 2**, while the maximum decomposition temperatures are observed at 439 °C and 452 °C for **Dye 1** and **Dye 2**, respectively. These excellent thermal properties indicate that both dyes are well suited for device fabrication processes, such as physical vapor deposition (PVD), and ensure sufficient thermal stability for OLED device operation.

Single crystal X-ray Diffraction Analysis

Single crystals of **Dye 1**, **Dye 2** and HHADBr were obtained by dissolving the compounds in a dichloromethane (DCM): methanol (MeOH) (1:4 v/v) mixture, followed by slow evaporation at room temperature. X-ray crystallographic data and refinement parameters are summarized in **Table S1**. **Dye 1** and **Dye 2** crystallized in the monoclinic crystal system with space groups of P 21/c and P2₁/n, respectively, whereas HHADBr is in the orthorhombic system with the Pbca space group. **Figure 2** represents the ORTEP diagrams (50% of the thermal ellipsoids) of **Dye 1**, **Dye 2** and HHADBr. Supramolecular interactions visualized in crystal packing are provided in **Figure S10.**

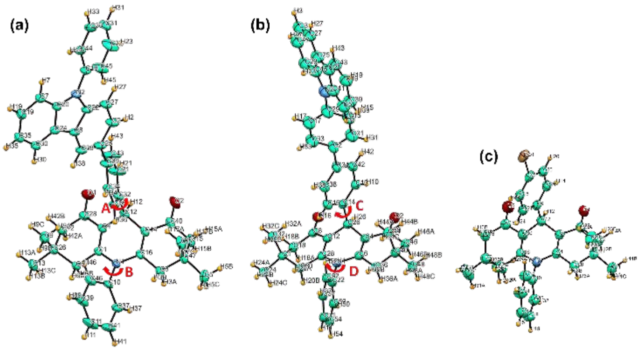

Figure 2. ORTEP diagrams of (a) **Dye 1**, (b) **Dye 2**, and (c) HHADBr, shown with 50% probability thermal ellipsoids, based on single-crystal X-ray diffraction data.

As shown in **Figure 2**, **Dye 1** exhibits a dihedral angle of 78.12° (A) between HHAD and the phenylene spacer and an angle of 89.74° (B) between the HHAD and its N-phenyl group. In contrast, **Dye 2** shows a dihedral angle of 81.40° (C) between HHAD and the phenylene spacer, and a dihedral angle of 62.10° (D) between HHAD and the N-phenyl group. These angular differences reflect conformational flexibility and molecular asymmetry. **Dye 1** revealed a diverse array of weak non-covalent interactions contributing to the overall crystal stability. Several close contacts were observed between carbon and hydrogen atoms, with C⋯H and H⋯H distances ranging from 1.592 Å to 2.945 Å, indicative of van der Waals interactions and possible weak hydrogen bonding. Notably, very short H⋯H distances such as H55⋯H47 (1.592 Å) and H7⋯H47 (1.949 Å) suggest dense molecular packing. Interactions such as O1⋯H48C (2.574 Å) and H24⋯H54 (2.36 Å) also imply the presence of weak hydrogen bonds that further stabilize the lattice. However, the centroid-to-centroid distances between aromatic carbazole and phenyl rings 5.217, 5.418, and 5.597 Å exceed the typical range for strong π-π stacking (3.3-3.8 Å), suggesting that classical face-to-face stacking is minimal. Instead, molecular packing is likely supported by slipped or edge-to-face aromatic interactions combined with a complex network of weak intermolecular contacts. **Dye 2** exhibits a dihedral angle between HHAD and CzPh (C4-C12-C32-C21) was -106.8° indicating a pronounced twist that precludes planarity and restricts through-bond conjugation. Between the phenyl spacer and the carbazole, the torsion angle C34-C29-C25-C2 measures 141.2°, suggesting a partially extended yet non-coplanar conformation. A near-perpendicular geometry of 78.4° (C20-N2-C18-C45) is observed between the carbazole and its 9H-position substituted phenyl ring, a conformation typically adopted to alleviate steric hindrance around the nitrogen. Additionally, the torsion angle of 115.5° (C46-C10-N1-C16) between HHAD and its N-phenyl further highlights the conformational flexibility of the system. These pronounced dihedral angles collectively illustrate the non-planar character of **Dye 2** compared to **Dye 1**, which likely arises from a compromise between intramolecular steric demands and the requirements of efficient molecular packing within the crystal lattice. In the **Dye 2** crystal structure, the interatomic distances reveal a network of weak but potentially significant non-covalent interactions (C-H⋯π and H⋯H) that contribute to the overall crystal packing. Together, the torsional distortions and intermolecular contacts suggest that crystal packing in **Dye 2** is driven by a delicate interplay of steric effects, disrupted conjugation and non-covalent interactions. The presence of N-phenyl substitution on HHAD in **Dye 2** enhances lattice stabilization by introducing steric bulk and rotational degrees of freedom that increase the number and diversity of weak intermolecular interactions. Furthermore, the spatial positioning of the Cz/CzPh unit significantly influences lattice organization: asymmetric attachment, as observed in **Dye 2**, induces torsional strain that disrupts conjugation but simultaneously enables the molecule to adopt favorable packing conformers. This facilitates denser crystal assembly through co-operative non-covalent interactions. The SCXRD analysis of HHADBr reveals several close contacts indicative of tight molecular packing. A weak hydrogen bond is observed between H26A and O3 (2.415 Å), while short H⋯H contacts such as H32⋯H12 (2.371 Å) and H21⋯H31C (2.347 Å) suggest close intermolecular proximity. Additional weak van der Waals interactions include H32⋯C12 (2.941 Å) and H19⋯C4 (2.888 Å). Notably, Br⋯H interactions (H17⋯Br01 at 3.024 Å and Br01⋯H2A at 3.057 Å) indicate halogen-involved contacts that contribute to lattice stabilization. Overall, the data reflects a densely packed and stabilized crystal structure. Moreover, in HHADBr, the dihedral angle between the hexahydroacridine ring and the C-substituted 4-bromophenyl unit is 89.92º, whereas the angle between the hexahydroacridine ring and the N-substituted phenyl group is 88.15º. These findings, along with the observed torsional flexibility and dihedral angles, highlight a structural framework stabilized predominantly by weak but spatially distributed supramolecular forces rather than strong directional interactions. These molecules are designed with a twisted donor-acceptor structure that helps them emit light efficiently through TADF, while weak π-π stacking prevents them from losing brightness when packed together (no ACQ). Their tight but non-planar packing adds rigidity, reducing energy loss. Altogether, these features make **Dye 1** and **Dye 2** strong candidates for bright, stable OLED displays and lighting with low efficiency loss.

Optoelectronic properties

UV-Vis and PL Properties: The photophysical properties of the two dyes were investigated using by UV-Vis absorption and PL spectroscopy in both dilute solutions and spin-coated thin films (**Table 1**). As shown in **Figure 3a**, the wavelength of maximum absorption ($\lambda_{max, abs}$) in THF (10^{-5} M) appeared at 256 for **Dye 1** and 294 nm for **Dye 2**, along with a weaker band near 320 nm, which are attributed to the local π→π* and n→π* transitions of the HHAD derivatives, respectively.[27] In addition, the low intensity absorption tail observed beyond ~350nm range is attributed to weak intramolecular charge transfer (ICT) transitions between the electron-donating Cz unit and the electron-accepting HHAD. In the solid state, the $\lambda_{max, abs}$ for the spin-coated films of dyes were found at 255 and 251 nm, respectively (**Figure 3c**). The optical band gaps (E_g^{opt}) of the dyes in thin film form were estimated from their excitation spectra (**Figure 3c**), and values are in the range of 2.66 to 2.98 eV (**Table 1)**. As illustrated in **Figure 3c**, both dyes emit blue light, with wavelengths of maximum emission ($\lambda_{max, em}$) at 466 nm (**Dye 1**), and 439 nm (**Dye 2**). Furthermore, they exhibit hypsochromic and bathochromic shifts depending on the solvent used. These spectral variations are likely attributable to differences in intermolecular aggregation, variations in the torsional angles of the phenyl units, and microenvironmental polarity, all of which influence molecular conformation, packing and electronic interactions in solution versus solid-state environments.[37] To investigate the changes in dipole moment upon excitation, the Stokes shifts were analyzed using Lippert-Mataga plots ($\Delta\nu$ vs Δf) as shown in **Figure S14**, with the extracted values listed in **Table S2**. In all solvents, **Dye 1** exhibited a larger Stokes shift than **Dye 2**, indicating that upon excitation, **Dye 1** undergoes more pronounced geometric or electronic relaxation before emission.[38,39] This behavior is likely attributed to the more flexible D-A architecture of **Dye 1**. The slope of the linear fit reflects the extent of dipole moment change between the ground and the excited states. **Dye 1** exhibited a higher slope (3533 cm^{-1}) than **Dye 2** (1436 cm^{-1}), indicating a stronger ICT character upon excitation and supporting the occurrence of electronic rearrangement.[40,41] This enhanced ICT behavior likely arises from the greater rotational freedom of **Dye 1**, which facilitates a more coplanar and efficient conjugation pathway between the donor and acceptor units in the excited state. Similarly, in the solid state, **Dye 1** also exhibited a much larger Stokes shift, indicating that it retains greater rotational freedom than **Dye 2**. These observations further support that **Dye 2** possesses a more rigid molecular architecture, which effectively suppresses vibrational energy loss, enhancing emission efficiency and leading to a shorter emission wavelength (i.e., purer blue emission) (**Table 1**).

View Article Online
DOI: 10.1039/D6TC01365K

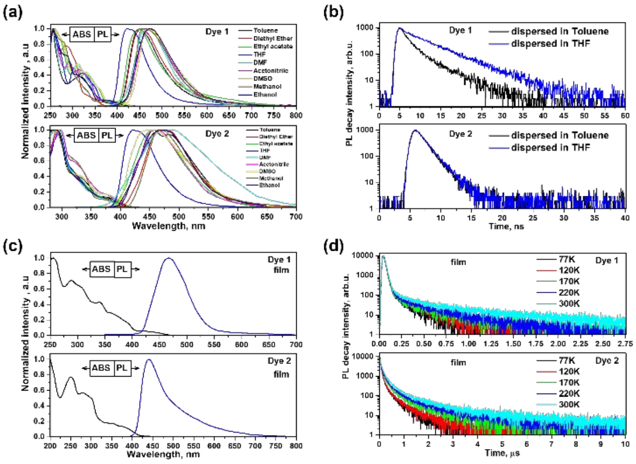

Figure 3. (a), (c) UV-Vis absorption and PL emission spectra of the dyes in various solutions and film, (b) PL decay profiles of the dyes in toluene and THF and (d) PL decay behavior of the films at different temperatures.

Frontier Energy Levels: To investigate the frontier energy levels, cyclic voltammetry (CV) measurement was performed on the compounds dissolved in dichloromethane (DCM) (**Figure S13** and **Table 1**). From the onset oxidation potentials, the HOMO energy levels or ionization potentials (IP_{CV}) were determined to be -5.72 eV, and -5.59 eV for **Dye 1** and **Dye 2**, respectively. These values agreed with the HOMO energy levels calculated using DFT. In addition, their electron affinity (EA_{CV}) values obtained from the CV plots were -3.06 and -2.61eV, respectively.

AIE Properties: The PLQYs of the spin-coated thin films were significantly higher than those measured in polar (THF) and non-polar (toluene) solutions (**Table 1**), indicating enhanced emission in the aggregated solid-state phase. To investigate this aggregation-induced enhancement, PL spectra were recorded in THF/water mixtures with increasing water fractions (0–95 %), as shown in **Figure 4**. As the water content increased, the photoluminescence intensity also increased, confirming the presence of AIE. This enhancement is attributed to the restriction of intramolecular motions (RIM) such as bond rotations and vibrations, which suppress non-radiative decay pathways.[42,43,44] In particular, for **Dye 1** (**Figure 4a**), as the water fraction increases (poor solvent, aggregation condition), the PL intensity rises sharply, reaching a maximum at around 70% water, and then decreases at higher water contents, this trend is a hallmark of gradual AIE. The observed color change is attributed to altered molecular packing and excited-state interactions in the aggregated state.[45,46] The rigid aggregated state also reduces molecular degradation, potentially improving the thermal and operational stability of these compounds in OLED applications.[47]

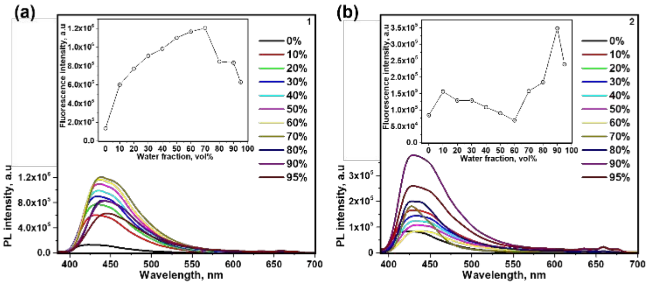

Figure 4. PL spectra and corresponding plots of the relative PL intensity of the dispersed (a) **Dye 1** and (b) **Dye 2** in THF/H_2O mixtures with different water volume fractions (f_w).

TADF Characteristics: To evaluate the behavior of TADF, the PL spectra of the dyes dissolved in toluene were measured at room temperature under air and N_2 (**Figure S17**). The PL intensity ratio $\left(\frac{PL_{air}}{PL_{No\ air}}\right)$ serves as an indicator of the TADF contribution, since oxygen efficiently quenches triplet excitons and suppresses delayed fluorescence. **Dye 2** exhibited the highest PL ratio of 16.54, strongly suggesting the most efficient TADF contribution via RISC from the triplet to the singlet state, consistent with literature report.[48] In addition, for the **Dye 2** solution in THF, the polar environment stabilizes the excited CT state, effectively reducing the non-radiative decay pathways and resulting in enhanced PLQY. In contrast, **Dye 1** exhibited an opposite trend, likely due to its weaker CT character in THF, as previously reported.[49,50] As shown in **Figure 3b**, the PL decay curves in solution are in the nanosecond range, which is characteristic of prompt fluorescence. However, in the films (**Figure 3d**), the decay extends into the microsecond range, which can be attributed to delayed fluorescence due to restricted molecular motion, enhanced ISC and triplet harvesting in the rigid solid-state matrix.[51] Moreover, decreasing the temperature results in shorter emission lifetimes, a key signature of the TADF mechanism. This behavior supports the involvement of RISC, through which triplet excitons are upconverted to the singlet state via a thermally activated process (also illustrated in **Figure S18**). The PL and phosphorescence (PH) spectra of the spin-coated neat films are presented in **Figure 5a**. The **ΔE_{ST}** values, calculated as the energy difference between the onsets of the singlet (S_1) and triplet (T_1) states, are found to be 0.07 eV for **Dye 1**, and 0.06 eV for **Dye 2**, respectively. These small values confirm that both dyes are capable of efficient TADF, as such narrow singlet-triplet energy gaps facilitate RISC from the local triplet state (^{3}LE) to the charge-transfer singlet state (^{1}CT) at room temperature.[52,53] To further verify that the emission behavior is governed by the TADF mechanism, power-dependent PL measurements were performed by varying the excitation pulse energy. As shown in **Figure 5b**, the PL spectra of the films excited at 350 nm exhibited a monotonic increase in emission intensity with increasing excitation power. Notably, the emission peaks remained unchanged in position, indicating no significant spectral shift. This stability suggests that exciton-exciton annihilation or aggregation effects are negligible within the tested power range. The log-log plots of PL intensity versus excitation power (**Figure 5c**) were linearly fitted for each dye to assess the nature of the emission process. **Dye 2** showed a larger slope (1.07) than **Dye 1** (0.96), implying a strong contribution from triplet-singlet up-conversion, which is a hallmark of efficient TADF under photoexcitation. Since both slopes are below 2, the emission does not involve triplet-triplet annihilation (TTA) or bimolecular/triplet fusion processes. These results confirm that the observed delayed fluorescence arises from a monomolecular process consistent with TADF, as previously reported.[54,55.]

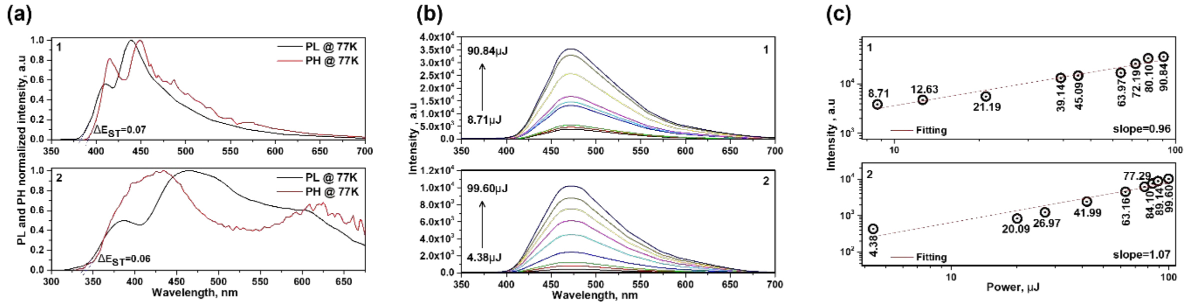

Figure 5. (a) PL and PH spectra of the dyes at 77 K and (b), (c) dependence of the emission intensity (measured with a delay of 50 μs after excitation) on the fluence of the excitation laser. The observed quadratic dependence indicates that the emission originates from a TADF process.

Förster and Dexter Energy Transfer: The Förster and Dexter energy transfer mechanisms represent two fundamental non-radiative energy transfer pathways between a host and a guest (or dopant), where the host typically serves as the energy donor and the dopant as the energy acceptor. Förster energy transfer occurs via long-range dipole-dipole interactions and requires spectral overlap between the PL spectrum of the host and the absorption spectrum of the guest. In contrast, Dexter energy transfer is a short-range process based on electron exchange, also dependent on spectral overlap and molecular orbital compatibility. To explore these mechanisms, bis[2-(diphenylphosphino)phenyl]ether oxide (DPEPO) was selected as the host material due to favorable emission characteristics, including a solid-state PL peak centered around 302 nm (**Figure S19**).[56,57] Additionally, DPEPO offers excellent thermal stability, and favorable electronic properties, including a HOMO energy level of ~ -6.1 eV, a LUMO energy level of ~ -2.0 eV, and high triplet energy level, making it a well-balanced host material for TADF emitters.[58] As summarized in **Table S3**, the PLQY of the host-guest films increased with the incorporation of DPEPO. The blend films containing 90 wt% DPEPO exhibited 1.55- and 1.42-fold enhancements in PLQY for **Dye 1** and **Dye 2**, respectively, compared to their neat films. The highest PLQY of 81% was obtained for the 10% **Dye 2**: 90% DPEPO blend. These improvements are attributed to the spatial separation of the emitter molecules in the host matrix, which suppresses π-π stacking, dexter energy transfer, and non-radiative decay simultaneously. Importantly, incorporation of DPEPO did not induce any notable blue or red shift in PL emission. As shown in **Figure 6a** and summarized in **Table 1**, the PL maxima remained stable, confirming that the emission color (blue) was retained and not significantly affected by host–guest interactions. Further insights into the host-guest interactions were obtained from the PL decay spectra (**Figure 6b**). The decay lifetimes (τ) increased with higher DPEPO content, as shown in **Table S4**, accompanied by a more pronounced delayed fluorescence component, particularly for **Dye 2**. This behavior

View Article Online
DOI: 10.1039/D6TC01665K

indicates more effective triplet harvesting, enhanced RISC, and possibly improved intermolecular interactions in the blend films. The RISC rate constants (k_{RISC}) for the 90 wt% DPEPO-blended films are 8.78×10^4 s^{-1} for **Dye 1** and 4.3×10^4 s^{-1} for **Dye 2**, respectively (**Table S5**). These findings are consistent with the small ΔE_{ST} values and align with previously reported TADF systems.[59]

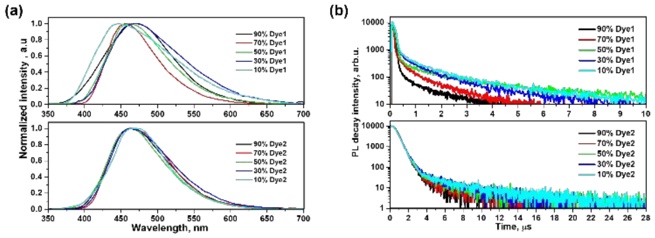

Figure 6. (a) and (b) PL decay spectrum (at room temperature) of spin-coated doped dyes using different concentrations of DPEPO as the host material.

OLED Device Performance

OLED devices using neat **Dye 1**, **Dye 2**, and their DPEPO-blended films as emissive layers (EMLs) were fabricated by physical vapor deposition (PVD). The device architecture (**Figure 7a**) was ITO/HATCN (15 nm)/TAPC (60 nm)/EML (10 nm)/TmPyPB (40 nm)/LiF/Al. Here, 1,4,5,8,9,11-hexaazatriphenylenehexacarbonitrile (**HATCN**) served as the hole injection layer (HIL), 1,1-bis[(di-4-tolylamino)phenyl]cyclohexane (TAPC) as the hole transport layer (HTL), and 1,3,5-tri(m-pyridin-3-ylphenyl)benzene (TmPyPB) as both the electron-transport and hole-blocking layer**.** Lithium fluoride (LiF) and aluminum (Al) were used as the electron-injection layer and cathode, respectively, while indium tin oxide (ITO) served as the transparent anode. The characteristics of representative OLED devices are shown in **Figures 7b-k** and **S20a,** and the key EL parameters are summarized in **Table 2.** All **Dye 2**-based devices exhibited markedly higher luminance (L) than their **Dye 1** counterparts. The maximum luminance values reached 27,786 cd.m^{-2} for **Dye 1** (90 wt% DPEPO) and 48,859 cd.m^{-2} for **Dye 2** (90 wt% DPEPO), consistent with their PLQY trends and the more efficient triplet-exciton utilization in **Dye 2.** At a DPEPO content of 90 wt%, balanced charge injection enables efficient conversion of excitons into radiative singlet states, while the high host concentration provides optimal intermolecular spacing that minimizes concentration quenching yet maintains efficient energy transfer.[60,61,62] The EL spectra of the devices closely match the PL spectra of the corresponding spin-coated films, confirming that the emissive species retain their optoelectronic properties within the device environment.

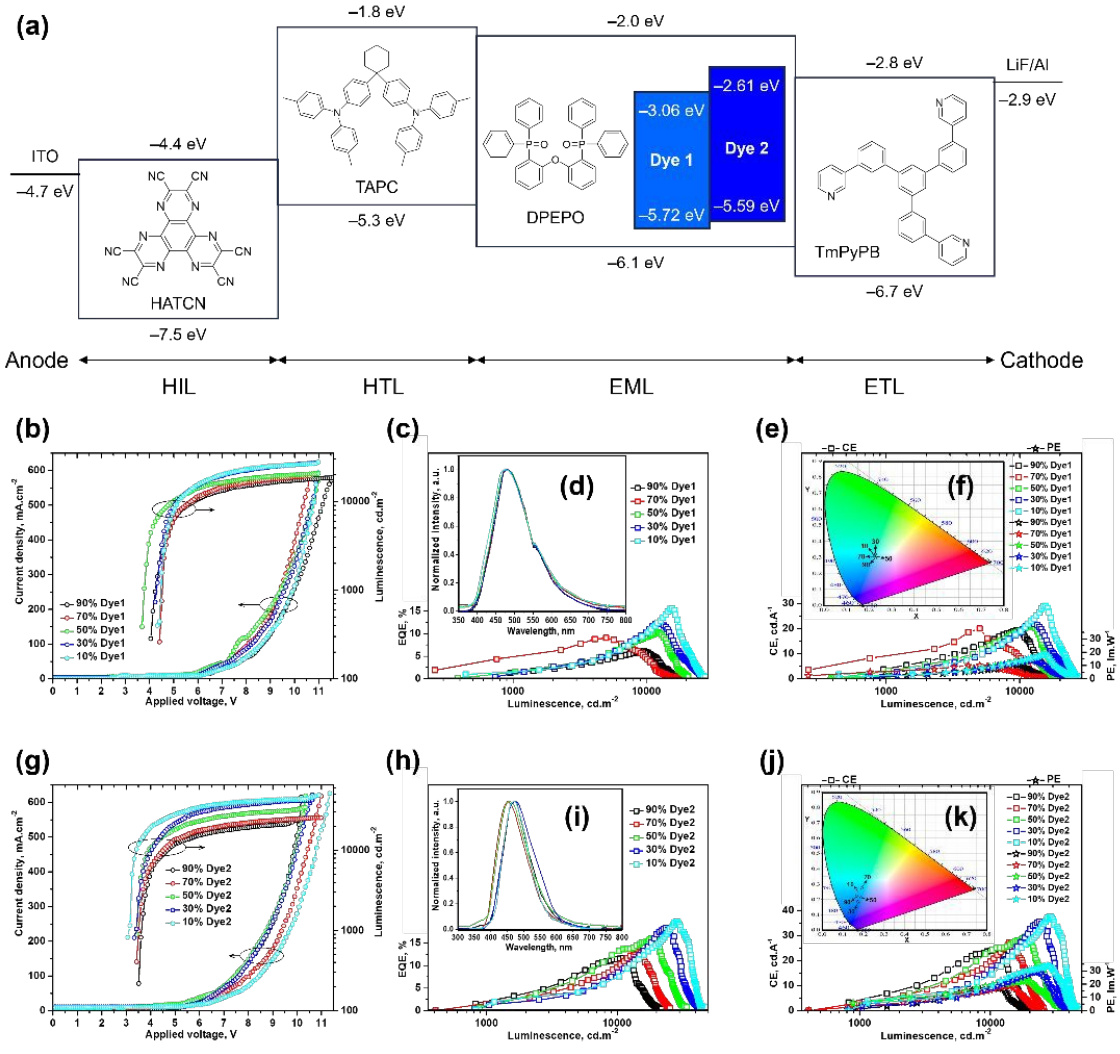

Figure 7. (a) The device architecture and energy-level diagram of the materials used in the TADF OLEDs. Device performance of OLEDs employing **Dye 1** in a DPEPO host at various doping concentrations: (b) current density and luminance versus applied voltage, (c) external quantum efficiency (EQE) versus luminance, (d) electroluminescence (EL) spectrum

View Article Online
DOI: 10.1039/D6TC01065K

recorded at 7 V, (e) current efficiency (CE) and power efficiency (PE) versus luminance, and (f) CIE chromaticity coordinates. Device performance of OLEDs employing **Dye 2** in a DPEPO host at various doping concentrations: (g) current density and luminance versus applied voltage, (h) EQE versus luminance, (i) EL spectrum recorded at 7 V, (j) CE and PE versus luminance, and (k) CIE chromaticity coordinates.

Interestingly, the OLED device containing 70 wt.% DPEPO and 30 wt.% Dye 2 exhibited a noticeable blue shift in the EL emission peak (452 nm) and corresponding CIE coordinates compared with the devices containing 90 wt.% and 50 wt.% DPEPO. This behavior is likely associated with changes in the local host–guest environment and molecular packing at this specific composition. The reduced intermolecular interactions and aggregation effects at the intermediate doping concentration may lead to a less stabilized charge-transfer excited state, resulting in higher excited-state energy and a blue-shifted emission. In addition, variations in exciton recombination zones and host–guest interactions can influence the emission characteristics, leading to the observed deviation in both EL wavelength and CIE coordinates. Similar concentration-dependent spectral variations have been reported in host–guest TADF systems and are commonly attributed to changes in molecular packing and excited-state interactions. Among devices with comparable EML thickness (~10 nm), the neat **Dye 2**-based OLED exhibits the lowest turn-on voltage (3.08 V) and the purest blue emission with CIE coordinates of (0.179, 0.183) **(Table 2).** Increasing the DPEPO concentration leads to enhanced external quantum efficiency (EQE), in agreement with the PLQY trend (**Table S3**), owing to improved exciton confinement, suppressed aggregation, and more efficient TADF emission.[63] The maximum EQE values are achieved at 90 wt% DPEPO, reaching 15.58% for **Dye 1** and 19.71% for **Dye 2**. The well-aligned HOMO and LUMO energy levels of the dyes and the DPEPO host facilitate balanced charge injection and reduce Joule heating, resulting in improved current efficiency (CE) and power efficiency (PE). Notably, all **Dye 2**-based devices significantly outperform their **Dye 1** counterparts, achieving a maximum CE of 37.66 cd.A^{-1} and PE of 33.73 lm.W^{-1}. This enhancement is primarily attributed to the more rigid molecular backbone of **Dye 2**, which effectively suppresses vibrational energy loss. Overall, these results highlight the synergistic effects of molecular design, host-guest energy alignment, and optimized device architecture. Comparison with reported blue TADF emitters (**Table S6**) demonstrates that these dyes achieve performance comparable to or exceeding state-of-the-art systems, underscoring their strong potential for high-efficiency blue OLED applications. In addition to the high maximum EQE values, the devices exhibited relatively low efficiency roll-off with increasing luminance. This behavior is mainly attributed to the small ΔE_{ST} values of Dye 1 and Dye 2, which promote efficient RISC and reduce triplet accumulation under device operation. The high PLQY of the emitters, together with the rigid and twisted molecular structures, suppresses non-radiative decay and aggregation-induced quenching. Moreover, the favorable host–guest energy alignment and balanced charge transport within the emitting layer reduce exciton-related loss pathways, including triplet–triplet annihilation (TTA) and triplet–polaron annihilation (TPA). Consequently, efficient exciton utilization is maintained even at elevated brightness levels, resulting in reduced efficiency roll-off and stable OLED performance.

Experimental Section

Synthesis of 9-(4'-(9H-carbazol-9-yl)-[1,1'-biphenyl]-4-yl)-3,3,6,6-tetramethyl-10-phenyl-3,4,6,7,9,10-hexahydroacridine-1,8(2H,5H)-dione (Dye 1): 9-(4-Bromophenyl)-3,3,6,6-tetramethyl-10-phenyl-3,4,6,7,9,10-hexahydroacridine-1,8(2H,5H)-dione (HHADBr) (200 mg, 0.4 mmol) and (4-(9H-carbazol-9-yl)phenyl)boronic acid (108 mg, 0.4 mmol) were dissolved into 15 mL of tetrahydrofuran (THF). 5 mL aqueous solution of K_2CO_3 (1.2 mmol) was then added, and the mixture was stirred for 30 min at room temperature. $Pd(PPh_3)_4$ (20 mol% over HHADBr) was added, and the mixture was heated to 80 ºC for 12 h under argon atmosphere. After cooling to room temperature, the mixture was quenched with 30 mL of water. The product was extracted with ethyl acetate (3×30 mL) and dried over Na_2SO_4. The solvent was removed under reduced pressure. The crude product was purified by silica gel column chromatography using hexane/ethyl acetate (1:1, v/v) as the eluent, affording **Dye 1** as a pale-yellow solid (yield: 48%). ^{1}H NMR ($CDCl_3$, 500 MHz) (ppm): δ 8.07 (d, J=5 Hz, 2H), 7.7 (d, J=10 Hz, 2H), 7.52-7.51 (m, 7H), 7.39-7.33 (m, 5H), 7.22 (t, J=10 Hz, 4H), 5.29 (s, 1H), 4.04 (q, J=10 Hz, 1H) 2.19-2.11 (m, 4H), 2.05-1.97 (m, 4H), 0.89 (s, 6H) and 0.78 (s, 6H). ^{13}C{^{1}H} NMR ($CDCl_3$, 125 MHz): δ 196.02, 149.89, 145.80, 140.91, 140.50, 139.12, 137.73, 136.38, 129.47, 128.53, 128.32, 127.20, 126.93, 125.93, 123.37, 120.28, 119.88, 114.54, 109.90, 50.24, 41.89, 32.63, 32.48, 29.76 and 26.84 ppm. HR-MS (m/z) $[C_{47}H_{42}N_2O_2]^+$: Calcd. 666.3246 found 667.3330 $[M+H]^+$.

View Article Online
DOI: 10.1039/D6TC01665K

Table 2. Summary of device performance parameters for fabricated non-doped and doped devices.

EML	Turn on V, (V)	Maximum L, (cd.m^{-2})	Maximum CE, (cd.A^{-1})	Maximum PE, (lm.W^{-1})	Maximum EQE, (%)	Maximum EL, nm	CIE (X, Y)
Dye 1	4.41	10122	8.99	5.10	1.98	448	(0.181, 0.200)
90% Dye 1	4.05	18558	19.17	8.86	6.03	481	(0.222, 0.312)
70% Dye 1	4.41	19312	20.02	10.02	9.02	479	(0.229, 0.322)
50% Dye 1	3.69	20609	21.20	14.29	10.22	478	(0.230, 0.313)
30% Dye 1	4.23	27045	22.08	14.14	12.21	478	(0.225, 0.318)
10% Dye 1	4.32	27786	29.14	18.07	15.58	473	(0.228, 0.299)
Dye 2	3.08	16082	23.25	16.27	7.90	440	(0.179, 0.183)
90% Dye 2	3.42	23858	24.25	17.33	11.65	473	(0.179, 0.241)
70% Dye 2	3.42	25469	27.15	19.23	13.40	452	(0.173, 0.189)
50% Dye 2	3.42	34307	29.52	22.62	16.04	458	(0.188, 0.215)
30% Dye 2	3.33	42340	35.41	29.14	18.35	472	(0.192, 0.277)
10% Dye 2	3.06	48859	37.66	33.73	19.71	469	(0.167, 0.225)

Synthesis of 3,3,6,6-tetramethyl-10-phenyl-9-(4-(9-phenyl-9H-carbazol-3-yl)phenyl)-3,4,6,7,9,10-hexahydroacridine-1,8(2H,5H)-dione (Dye 2): HHADBr (200 mg, 0.4 mmol) and (9-phenyl-9H-carbazol-3-yl)boronic acid (108 mg, 0.4 mmol) were dissolved in 15 mL of THF. 5 mL aqueous solution of K_2CO_3 (1.2 mmol) was added, and the mixture was stirred for 30 min at room temperature. $Pd(PPh_3)_4$ (20 mol% over HHADBr) was then introduced, and the mixture was heated to 80 ºC for 12 h under argon atmosphere. After cooling to room temperature, the reaction was quenched with 30 mL of water and extracted with ethyl acetate (3×30 mL). The combined organic layers were dried over Na_2SO_4, and the solvent was removed under reduced pressure. The crude product was purified by silica gel column chromatography using hexane/ethyl acetate (1:1, v/v) as the eluent to afford **Dye 2** as a yellow-orange solid (yield: 41%). ^{1}H NMR ($CDCl_3$, 500 MHz) (ppm): δ 8.24 (s, 1H), 8.08 (d, J=10 Hz, 1H), 7.55-7.48 (m, 12H), 7.38-7.33 (m, 4H), 7.22-7.17 (m, 3H), 5.28 (s, 1H), 2.17-2.00 (m, 6H), 1.77 (d, J=20 Hz, 2H), 0.88 (s, 6H) and 0.77 (s, 6H). $^{13}C\{^1H\}$ NMR ($CDCl_3$, 125 MHz): δ 195.99, 149.79, 144.66, 141.28, 140.16, 139.47, 139.17, 137.75, 133.74, 129.90, 129.43, 128.36, 127.44, 127.10, 127.06, 125.99, 124.50, 123.78, 123.59, 120.34, 119.97, 118.65, 114.68, 109.87, 50.28, 41.87, 32.48, 29.75 and 26.94 ppm. HR-MS (m/z) $[C_{47}H_{42}N_2O_2]^+$: Calcd. 666.3246 found 667.3327 $[M+H]^+$.

Conclusion

Achieving stable and efficient blue OLED emitters requires molecular systems that can simultaneously support high-energy emission, efficient triplet utilization, and suppression of nonradiative decay in the solid state. This work identifies the saturated HHAD unit as a novel and effective acceptor building block that addresses several of these long-standing challenges at the materials level. Unlike conventional planar acceptors, HHAD introduces intrinsic conformational rigidity and steric modulation while maintaining strong electron-withdrawing character through its diketone functionality. By controlling donor–acceptor linkage topology, we demonstrate how conformational restriction governs aggregation behavior, excited-state relaxation, and delayed fluorescence efficiency. The resulting HHAD-based emitters exhibit aggregation-induced emission, small singlet-triplet energy gaps, and efficient reverse intersystem crossing, confirming that rigid, nonplanar acceptor architectures can overcome the efficiency losses typically associated with deep blue TADF systems. Device results further validate these molecular design principles, with the optimized emitter delivering pure blue light, high efficiency, high luminance, and low turn-on voltage. Overall, this study expands the acceptor design space for blue TADF materials and establishes HHAD as a versatile platform for developing next-generation blue emitters that balance efficiency, color purity, and solid-state stability.

Author contributions

Ms. Mageshwari Anandan: Writing draft, Synthesis of dyes, characterization, photophysics

Dr. Sohrab Nasiri:Manuscript writing, photophysical characterization, and electroluminescence

Dr. Praveen B. Managutti: Single crystal X-ray data analysis

Dr. Sharmarke Mohamed: Single crystal X-ray data analysis

Prof. Juozas Padgurskas: Density Functional Theory (DFT) calculations

Prof. Raimundas Rukuiza: Density Functional Theory (DFT) calculations

Prof. Jean Michel Nunzi: Device fabrication and testing, funding

Dr. Venkatramaiah Nutalapati: Conceptualization, supervision, funding acquisition and project administration

Prof. Yuning Li: Conceptualization, supervision, funding acquisition and project administration

View Article Online
DOI: 10.1039/D6TC01665K

Conflicts of interest

The authors declare no conflict of interest.

Data availability

The data that support the findings of this study are available from the corresponding author upon reasonable request.

Acknowledgements

This work was partially supported by the Natural Sciences and Engineering Research Council of Canada (NSERC) through the NSERC Alliance-Missions (ALLRP 586639-2023) and the Discovery Grants (RGPIN-2022-03835). Furthermore, this work was partially supported by a project funded by the Research Council of Lithuania (LMTLT) under Grant Agreement No. S-PD-24-174. NVR thank to SRM University-AP for the seed grant (SRM AP/URG/Research/SEED/2026-27/009).

References

1. S. J. Zou, Y. Shen, F. M. Xie, J. D. Chen, Y. Q. Li and J. X. Tang, *Mater. Chem. Front*., 2020, **4**, 788–820.
2. T. Hatakeyama, K. Shiren, K. Nakajima, S. Nomura, S. Nakatsuka, K. Kinoshita, J. Ni, Y. Ono and T. Ikuta, *Adv. Mater*., 2016, **28**, 2777–2781.
3. Y. Kondo, K. Yoshiura, S. Kitera, H. Nishi, S. Oda, H. Gotoh, Y. Sasada, M. Yanai and T. Hatakeyama, *Nat. Photonics*, 2019, **13**, 678–682.
4. L. T. Sharpe, A. Stockman, W. Jagla and H. Jägle, *J. Vis*., 2005, **5**, 11, 948–968..
5. E. Tankelevičiūtė, I. D. W. Samuel and E. Zysman-Colman, *J. Phys. Chem. Lett*., 2024, **15**, 1034–1042.
6. A. Farokhi, S. Lipinski, L. M. Cavinato, H. Shahroosvand, B. Pashaei, S. Karimi, S. Bellani, F. Bonaccorso and R. D. Costa, *Chem. Soc. Rev.,* 2025, **54**, 266–340.
7. G. Hong, X. Gan, C. Leonhardt, Z. Zhang, J. Seibert, J. M. Busch and S. Bräse, *Adv. Mater*., 2021, **33**, 2005630.
8. Q. Y. Meng, R. Wang, Y. L. Wang, X. W. Guo, Y. Q. Liu, X. L. Wen, C. Y. Yao and J. Qiao, *Nat. Commun*., 2023, **14**, 1, 3927.
9. S. Izawa, M. Morimoto, K. Fujimoto, K. Banno, Y. Majima, M. Takahashi, S. Naka, M. Hiramoto, *Nat. Commun*., 2023, **14**, 5494.
10. X. Cai, S. J. Su, *Adv. Funct. Mater.,* 2018, **28**, 1802558.
11. X. L. Chen, J. H. Jia, R. Yu, J. Z. Liao, M. X. Yang, C. Z. Lu, *Angew. Chem. Int. Ed*., 2017, **56**, 15006–15009
12. L. S. Cui, H. Nomura, Y. Geng, J. U. k. Kim, H. Nakanotani, C. Adachi, *Angew. Chem. Int. Ed*.,2017, **56**, 6, 1571-1575.
13. H. Nakanotani, T. Higuchi, T. Furukawa, K. Masui, K. Morimoto, M. Numata, H. Tanaka, Y. Sagara, T. Yasuda, C. Adachi, , *Nat. Commun*., 2014*,* **5***,* 1 , 4016.
14. C. Y. Chan, L. S. Cui, J. U. Kim, H. Nakanotani, C. Adachi, *Adv. Funct. Mater.,* 2018, **28**, 1706023.
15. M. Liu, Y. Seino, D. Chen, S. Inomata, S. J. Su, H. Sasabe, J. Kido, *Chem. Comm.,* 2015, **51**, 16353-16356.
16. J. M. Dos Santos, D. Hall, B. Basumatary, M. Bryden, D. Chen, P. Choudhary, T. Comerford, E. Crovini, A. Danos, J. De, S. Diesing, M. Fatahi, M. Griffin, A. K. Gupta, H. Hafeez, L. Hämmerling, E. Hanover, J. Haug, T. Heil, D. Karthik, S. Kumar, O. Lee, H. Li, F. Lucas, C. F. R. Mackenzie, A. Mariko, T. Matulaitis, F. Millward, Y. Olivier, et al., *Chem. Rev.,* 2024, **124**, 13736-14110.
17. H. J. Tan, G. X. Yang, Y. L. Deng, C. Cao, J. H. Tan, Z. L. Zhu, W. C. Chen, Y. Xiong, J. X. Jian, C. S. Lee, Q. X. Tong, *Adv. Mat.,* 2022, **34**, 2200537.
18. D. H. Ahn, S. W. Kim, H. Lee, I. J. Ko, D. Karthik, J. Y. Lee, J. H. Kwon, *Nat. Photonics,* 2019*,* **13,** 8, 540-546.
19. L. S. Cui, A. J. Gillett, S. F. Zhang, H. Ye, Y. Liu, X. K. Chen, Z. Sen Lin, E. W. Evans, W. K. Myers, T. K. Ronson, H. Nakanotani, S. Reineke, J. L. Bredas, C. Adachi, R. H. Friend, *Nat. Photonics,* 2020*,* **14**, 10, 636-642.
20. Q. Liu, Y. Deng, B. Ren, X. Lan, Y. Zhang, R. Guo, C. Li, G. Xiong, Y. Sun, Z. Zhao, *Nanomaterials,* 2023, ***13***, 2517.
21. G. D. Zou, C. B. Duan, S. W. Lu, X. H. Zhao, Q. L. Du, H. Xu, J. F. Zhao, L. H. Xie, X. W. Zhang, D. J. Deng, *J. Lumin.,* 2022, **243**, 118595.
22. H. Nakanotani, T. Higuchi, T. Furukawa, K. Masui, K. Morimoto, M. Numata, H. Tanaka, Y. Sagara, T. Yasuda, C. Adachi, *Nat. Comm.,* 2014 **5***,* 4016.
23. S. Xiao, Y. Gao, R. Wang, H. Liu, W. Li, C. Zhou, S. Xue, S. T. Zhang, B. Yang, Y. Ma, *Chem. Eng. J.,* 2022, **440**, 135911.
24. A. Ilangovan, S. Malayappasamy, S. Muralidharan, S. Maruthamuthu, *Chem. Cent. J.,* 2011, **5**, 81.
25. M. A. Tehfe, F. Dumur, E. Contal, B. Graff, D. Gigmes, J. P. Fouassier, J. Lalevée, *Macromol. Chem. Phys.,* 2013, **214**, 19, 2189-2201.
26. N. Srividya, P. Ramamurthy, V. T. Ramakrishnan, *Spectrochim. Acta A Mol. Biomol. Spectrosc.,* 1998, **54**, 245-253.
27. M. Anandan, S. Kment, R. Zboril, S. Kalytchuk, G. Janusas, P. B. Managutti, S. Mohamed, R. Mazloumihaghghi, M. Hosseinnezhad, J. M. Nunzi, V. Nutalapati, S. Nasiri, *Org. Electron.,* 2025, **136**, 107162.
28. Y. Fu, H. Liu, B. Z. Tang, Z. Zhao, *Nat. Comm.,* 2023, **14**, 2019.
29. J. Wang, Y. Niu, Y. Jiang, Z. Chen, C. Yao, W. Yao, M. He and J. Zhang, Mater. Today Chem., 2025, 47, 102796.
30 T. Furukawa, H. Nakanotani, M. Inoue, C. Adachi, *Sci. Rep.,* 2015 **5**, 8429.
31. R. Kaçar, R. B. Serin, E. Uçar, M. Artuç, A. Ülkü and B. Kınacı, *Next Nanotechnol.,* 2025, **7**, 100132.
32. H. Cho, C. W. Byun, C. M. Kang, J. W. Shin, B. H. Kwon, S. Choi, N. S. Cho, J. I. Lee, H. Kim, J. H. Lee, M. Kim and H. Lee, *J. Inf. Disp.*, 2019, **20**, 249-255.
33. P. J. Stephens, F. J. Devlin, C. F. Chabalowski and M. J. Frisch*, J. Phys. Chem*., 1994, **98**, 11623–11627.
34. J. Wang, Y. Yang, F. Gu, X. Zhai, C. Yao, J. Zhang, C. Jiang and X. Xi, *ACS Appl. Mater. Interfaces*, 2023, **15**, 59643–59654.
35. B. R. Kaafarani, A. O. El-Ballouli, R. Trattnig, A. Fonari, S. Sax, B. Wex, C. Risko, R. S. Khnayzer, S. Barlow, D. Patra, T. V. Timofeeva, E. J. W. List, J. L. Brédas and S. R. Marder, *J. Mater. Chem. C Mater.*, 2013, **1**, 1638–1650.
36. P. K. Samanta, D. Kim, V. Coropceanu and J. L. Brédas, *J. Am. Chem. Soc.*, 2017, **139**, 4042–4051.
37. B. K. Sharma, A. M. Shaikh, R. M. Kamble, *J. Chem. Sci.,* 2015, **127**, 2063-2071.

38. F. Zhang, B. Liu, G. Liu, Y. Zhang, J. Wang, S. Wang, *Sci. Rep.,* 2018, **8,** 3131.
39. Y. Chen, J. Zhao, H. Guo and L. Xie, J. Org. Chem., 2012, 77, 2192-2206.
40. B. Czaplińska, K. Malarz, A. Mrozek-Wilczkiewicz, A. Słodek, M. Korzec and R. Musioł, *Molecules*, 2020, **25**, 2488.
41. S. Wu, Z. Ban, H. Tang, N. Ma, X. Ran, Q. Zhou, Y. Zhang, Z. Wang and X. Yu, *Chem. Commun*., 2025, **61**, 10574-10577.
42. H. Tang, J. Gao, L. Zhang, X. Li, Y. C. Duan, L. Wen, X. Liu, Z. M. Su, *New J. Chem.,* 2024, **48**, 19811.
43. D. Liu, J. Y. Wei, W. W. Tian, W. Jiang, Y. M. Sun, Z. Zhao, B. Z. Tang, *Chem. Sci.,* 2020, **11**, 7194.
44. G. R. Suman, M. Pandey and A. S. J. Chakravarthy, *Mater. Chem. Front.*, 2021, **5**, 1541-1584.
45. Y. Hong, J. W. Y. Lam and B. Z. Tang, *Chem. Soc. Rev*., 2011, **40**,5361-5388.
46. C. Y. K. Chan, J. W. Y. Lam, Z. Zhao, S. Chen, P. Lu, H. H. Y. Sung, H. S. Kwok, Y. Ma, I. D. Williams and B. Z. Tang, *J. Mater. Chem. C*, 2014, **2**, 4320-4327.
47. W. Zhang, S. Li, Y. Gong, J. Zhang, Y. Zhou, J. Kong, H. Fu and M. Zhou, *Angew. Chem., Int. Ed*., 2024, **63**, e202404978.
48. H. Yersin, Highly Efficient OLEDs: Materials Based on Thermally Activated Delayed Fluorescence, Wiley-VCH Verlag GmbH & Co. KGaA, Weinheim, Germany, 2018.
49. M. K. Etherington, F. Franchello, J. Gibson, T. Northey, J. Santos, J. S. Ward, H. F. Higginbotham, P. Data, A. Kurowska, P. L. Dos Santos, D. R. Graves, A. S. Batsanov, F. B. Dias, M. R. Bryce, T. J. Penfold and A. P. Monkman, *Nat. Commun.,* 2017, **8**, 14987.
50. M. Okazaki, Y. Takeda, P. Data, P. Pander, H. Higginbotham, A. P. Monkman, S. Minakata, *Chem. Sci.,* 2017, **8**, 2677-2686.
51. H. Tanaka, K. Shizu, H. Nakanotani and C. Adachi, *J. Phys. Chem. C*, 2014, **118**, 15985-15994.
52. S. H. Choi, C. H. Lee, C. Adachi and S. Y. Lee, *Dyes Pigm*., 2019, **171**, 107775.
53. J. Wang, J. Zhang, C. Jiang, C. Yao and X. Xi, *ACS Appl. Mater. Interfaces*, 2021, **13**, 57713–57724.
54. G. Li, R. S. Nobuyasu, B. Zhang, Y. Geng, B. Yao, Z. Xie, D. Zhu, G. Shan, W. Che, L. Yan, Z. Su, F. B. Dias, M. R. Bryce, *Chem. Eur. J.,* 2017, **23**, 11761-11766.
55. S. Nasiri, M. Rabiei, H. Shaki, M. Hosseinnezhad, K. Kalyani, A. Palevicius, A. Vilkauskas, G. Janusas, V. Nutalapati, S. Kment, J. Michel Nunzi, *J. Photochem. Photobio.l A Chem.,* 2024, **447**, 115289.
56. I. H. Lee, W. Song, J. Y. Lee, S. H. Hwang, *J. Mater. Chem. C.,* 2015, **3**, 8834.
57. W. Song, J. Y. Lee, *J. Phys. D App.l Phys.,* 2015, **48**, 365106.
58. C. Han, Y. Zhao, H. Xu, J. Chen, Z. Deng, D. Ma, Q. Li and P. Yan, *Chem. Eur. J.,* 2011, **17**, 5800-5805.
59. Q. Zhang, T. Komino, S. Huang, S. Matsunami, K. Goushi and C. Adachi, *Adv. Funct. Mater*., 2012, **22**, 2327-2336.
60. J. Y. Lee, *J. Inf. Disp*., 2014, **15**, 139-144.
61. S. K. Jeon and J. Y. Lee, *Org. Electron.,* 2020, **76**, 105477.
62. M. Zhang, W. Liu, C.-J. Zheng, K. Wang, Y.-Z. Shi, X. Li, H. Lin, S.-L. Tao and X.-H. Zhang, *Adv. Sci.,* 2019, **6**, 1801938.
63. C. Riley, H. H. Cho, A. C. Brannan, N. Le Phuoc, M. Linnolahti, N. C. Greenham and A. S. Romanov, *Commun. Chem.,* 2024, **7**, 298.